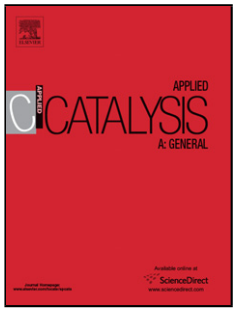

Title: Positional influence of Ru on Perovskite structured catalysts for efficient H_2 production process by heavy-hydrocarbon source

Authors: Yukwon Jeon, Ohchan Kwon, Chanmin Lee, Gicheon Lee, Jae-ha Myung, Sang Sun Park, John T.S. Irvine, Yong-gun Shul

PII: S0926-860X(19)30265-0
DOI: https://doi.org/10.1016/j.apcata.2019.117111
Article Number: 117111

Reference: APCATA 117111

To appear in: *Applied Catalysis A: General*

Received date: 10 March 2019
Revised date: 3 June 2019
Accepted date: 12 June 2019

Please cite this article as: Jeon Y, Kwon O, Lee C, Lee G, Myung J-ha, Sun Park S, Irvine JTS, Shul Y-gun, Positional influence of Ru on Perovskite structured catalysts for efficient H_2 production process by heavy-hydrocarbon source, *Applied Catalysis A, General* (2019), https://doi.org/10.1016/j.apcata.2019.117111

Positional influence of Ru on Perovskite structured catalysts for efficient H_2 production process by heavy-hydrocarbon source

Yukwon Jeon[a,b,†], *Ohchan Kwon*[b,†], *Chanmin Lee*[c], *Gicheon Lee*[b], *Jae-ha Myung*[d], *Sang Sun Park*[b], *John T. S. Irvine*[a] *and Yong-gun Shul*[b,*]

[a] *School of chemistry, University of St Andrews, St Andrews, Fife KY16 9ST, United Kingdom.*

[b] *Department of Chemical and Biomolecular Engineering, Yonsei University, 50 Yonsei-ro, Seodaemun-gu, Seoul, 03722, Republic of Korea.*

[c] *Research Institute of Sustainable Manufacturing System, Intelligent Sustainable Materials R&D Group, Korea Institute of Industrial Technology (KITECH), 89 Yangdaegiro-gil, Ipjang-myeon, Seobuk-gu, Cheonan-si, Chungcheongnam-do, 31056, Republic of Korea.*

[d] *Department of Materials Science and Engineering, Incheon National University, 119 Academy street, Songdo 1-dong, Yeonsu-gu, Incheon, 22012, Republic of Korea.*

†These authors contributed equally to this work.

*Corresponding author: Yong-Gun Shul

E-mail: shulyg@yonsei.ac.kr

Tel.: +82-2-2123-2758, Fax: +82-02-2123-3554

Table of Contents Graphic

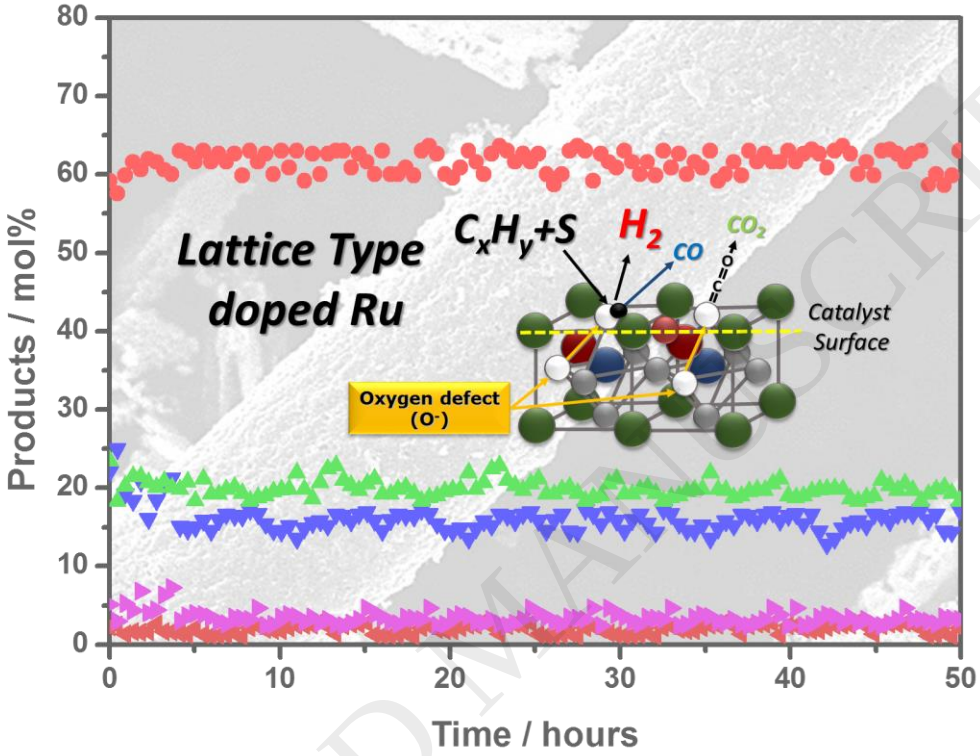

Highlights

- Perovskites for direct conversion of heavy-hydrocarbon source into H_2–rich gas fuels
- Lattice and Surface type Ru were designed by changing the position and loading
- Positional and chemical changes of Ru species affected to the reaction mechanism
- Lattice doped Ru shows great activity with less coke formation/sulfur poisoning

ABSTRACT

Direct conversion of heavy-hydrocarbon source into H_2–rich gas fuels has been highlighted as an efficient ultraclean system. Dictating the productivity of the system, the most important factor lies with the activity and physical/chemical stability of the catalytic materials. In this work, perovskite hollow fiber catalysts by partial substitution of Cr with Ru in the B site for $LaCrO_3$ ($LaCr_{1-x}Ru_xO_3$, x=0–0.4) are designed to investigate the effects of the positional and chemical changes of Ru on the catalytic properties at autothermal reforming of heavy-hydrocarbon. From a novel synthesis method, a hollow fibrous perovskite nanoparticle network is prepared to provide high surface area. Depending on the Ru doping levels, the optimal Ru amount exists as lattice type Ru, while an excess Ru resulted in the formation of surface type Ru on the perovskite. Especially, a slight structural modification of the orthorhombic structure owing from the doped Ru results in the increase of the surface oxygen and reducibility due to the high-valanced Cr and Ru states. After autothermal reforming of heavy-hydrocarbon including sulfur, it is obvious that the mixed lattice and surface Ru type shows a large deactivation due to the strong binding energy with carbon and sulfur. In contrast, less coke formation and sulfur poisoning are revealed for the catalyst with mostly lattice type Ru through the stable Ru species and high amount of active oxygen. Consequently, the hollow perovskite fiber catalyst of $LaCr_{0.8}Ru_{0.2}O_3$ displays the optimal activity to extract the highest amount of H_2 from the heavy-hydrocarbon source with exceptional stability.

KEYWORDS: Perovskite catalyst • Ru position • Stability • H2 production • coke/sulfur resistance

1. Introduction

Hydrogen (H_2) holds great promise as a fuel owing to the increasing demand for alternative energy sources such as new chemical processes and fuel cell systems.[1] Among many technologies used for producing H_2, reforming of fossil fuels is the most practical method because of its high energy efficiency. Heavy-hydrocarbon source, like diesel or gasoline, is one of the fuel candidate to practically establish H_2 infrastructure due to its rich H_2 content with high gravimetric and volumetric energy densities, easy storage and transport with accessibility.[2] The technology development to extract H_2 from heavy-hydrocarbons could also aid in the transition to use new energy sources such as gas oil, bio-oil and biomass etc. Autothermal reforming (ATR), a combination of steam reforming and partial oxidation reactions, has been widely studied for H_2 production from heavy-hydrocarbons due to its high yields of H_2 with low coke formation and fast reaction start-up, etc.[3] However, the main problem is the decrease in catalyst stability caused by an agglomeration of the metal active sites, sulfur poisoning and carbon coking, especially in such severe operating conditions.[4] Thus, high-efficiency H_2 production is mainly dependent on the catalyst design including catalytic activity/stability and resistance to the deposited carbon and sulfur. Precious metals, including Pt, Rh, Ru, and Pd, are typically used as catalysts deposited onto carefully engineered supports.[5] However, more catalyst studies are still needed to alleviate the significant deactivations in heavy-hydrocarbon reforming.

In recent years, perovskite catalysts have been investigated as candidates in the H_2 production reactions, due to their stability at high temperature, redox, and H_2-rich environments.[6] In addition, perovskites are resistant to coke deposition and have a low chemical binding energy with sulfur, which make them suitable for heavy-hydrocarbon reforming. Meanwhile, the compound of $LaCrO_3$ is a promising catalyst owing to its structural stability and good reducibility.[7] Perovskites have the formula ABO_3, where the B cation is believed to be

responsible for the catalytic activity. Also, cation A stabilizes the oxidation state of cation B, which can evenly disperse the active phase at the B-site throughout the perovskite material.[8] To further improve the activity and stability, partial substitution of B-sites by small amounts of other cations can alter the structure and electronic configuration of the perovskites.[5,9] The development of tailored functional materials that consist the catalytic nanoparticles on external surfaces or on inner lattices of porous crystals are also a key importance in the catalysis field.[10] In the case of sulfur poisoning and carbon coking, they usually take place on the active metal species by a strong chemical bonding with S and C.[11] Therefore, there is an issue on controlling the doped active metals in the perovskite structure compared to the deposited catalysts. However, not many studies have been dealt with the location of the substituted metal to the perovskite structure associated with the better reforming activity/stability and these mechanisms.

Here, as Ru is one of the most active and stable ingredients at the H_2 production reactions, Ru-substituted perovskite hollow fibers with the formula $LaCr_{1-x}Ru_xO_3$ (x=0-0.4) have been designed for an autothermal reforming catalyst to produce H_2 from model diesel fuel. The perovskite catalysts were prepared by an ACF (Activated carbon fiber) templating method to synthesize hollow fiber architectures with multi-mixed perovskite nanoparticles for an efficient heat/mass transfer including short diffusion and high contact time with the reactants in the autothermal reforming system.[12] Different catalytic behaviours of the heavy-hydrocarbon ATR were investigated by differentiating the structural and chemical states in the perovskite, which were characterized by the means of SEM/TEM, XRD, XPS, H2-TPR, XANES spectra, and EXAFS spectra. The initial activities of the designed perovskite catalysts were then measured, and each stability was compared in terms of the structural changes, carbon coking and sulfur poisoning

after ATR by heavy-hydrocarbon source. From the results, reaction mechanisms for both lattice and surface Ru type perovskites are investigated.

2. Results and Discussion

2.1 Ru doped hollow perovskite fibers

In Fig.1A, the hollow perovskite fibers with a composition of a perovskite nanoparticle network were successfully produced for each $La^{III}Cr^{III}_{1-x}Ru^{III}_{x}$/ACF composites, by a mild heat treatment at 1027 K under air flow to combust the carbon content.[12] The chemical compositions of the synthesized samples (Table 1) were found to agree well with the intended $LaCr_{1-x}Ru_xO_3$ compositions (x = 0, 0.05, 0.1, 0.2, 0.3 and 0.4), which are denoted as LC and LCR-x. SEM images clearly portray the obtained perfect micro-tubular features with uniform size and length (See details in Fig. S1), which is known to provide larger specific surface area than the perovskite grains prepared by the absence of an ACF template.[12a,b] An interesting finding is shown from the magnified SEM image of the hollow fiber surfaces (Fig. S1). The sizes of the spherical nanoparticles connected to the micro-tubular feature were seen to vary by the amount of Ru. This behaviour correlated well with the powder X-ray diffraction (XRD) results of the calculated average particle sizes, as summarized in Table 1, which shows a remarkable decrease from the LC to LCR-x (x = 0-0.2) samples. Pore volumes, BET surface areas, and average pore diameters were also calculated from N_2 adsorption–desorption isotherms (Table 1). As small mean crystallite sizes should be related to the total pore volume and surface area, it was found that the pore volume and surface area of the perovskites increased by the incorporation of Ru into the perovskite lattice. On the other hand, particles size increase was clearly shown with higher Ru ratios of 0.3 and 0.4, which may be due to the excess Ru agglomeration outside the perovskite surface. Among all, the

perovskite hollow fiber catalyst of LCR-0.2 showed an optimized high BET surface area of 14.4 m^2/g, which may support the catalytic reaction in the heavy-hydrocarbon ATR.

Homogeneity and the high crystallinity of the samples have been confirmed according to the XRD patterns in Fig.1B. These all showed the major diffraction peaks at similar angles, corresponding to the (hkl) indices of (112), (022), (220), (222), (312), and (040). These reflections correspond to those for the orthorhombic structure of $LaCrO_3$ perovskite with monoclinic La_2O_3 peaks within the *Pbnm* space group, reported in powder diffraction file JCPDF 024-1016.[9b,13] Unsubstituted $LaCrO_3$ has a structure with only one distinct B-site, whereas Ru doping introduces a monoclinic distortion into the ideally orthorhombic perovskite structure.[8] This reduction in symmetry creates two distinct B-sites that allow the cation to sit on two sites with slightly different bond lengths to the neighbouring oxygen atoms. From the magnified image of the (112) reflection at the right-hand side of Fig.1B, substitution of Ru^{III} into $LaCrO_3$ caused peak shifts to a lower angle but does not indicate significant changes in the perovskite structure. Also, an increased basal spacing (d-value) from 2.739 Å to 2.765 Å as well as changes in the unit cell parameter and volume can be observed (Table 1). The d-values were consistent with the basal spacing observed in the TEM images of the perovskite surfaces (Fig.S2) also increases in the length of a, b, and c axes in the unit cell were seen. The a, b, c axis increased from 5.499 to 5.519 Å (Δa = 0.020 Å), from 5.485 to 5.511 Å (Δb = 0.026 Å) and from 7.762 to 7.791 Å (Δc = 0.029 Å), respectively. These changes can be recognized as a partial B-site substitution due to the different crystal ionic radii of Cr^{III} (0.755 Å) and Ru^{III} (0.820 Å).[14] Such lattice expansion indicates that the crystal structure may contain a high percentage of octahedral RuO_6 configuration sites at the designed stoichiometric ratios.

2.2 Lattice and Surface type Ru

Meanwhile, in any of the XRD patterns (Fig.1B) of the prepared catalysts with the Ru fraction between 0.05–0.2 exhibited no additional phases. This result could be indicative of the existence of the Ru in the perovskite lattice structure. However, when the fraction of Ru was 0.3–0.4, monoclinic diffraction with individual peaks were observed with a decrease in the intensity of the perovskite structure. The individual metal oxide structures were mainly the formation of tetrahedral RuO_2 (JCPDS 083-1344),[15] which may be explained by the excess Ru deposited on the perovskite surface as separated Ru species. Based on the XRD analysis, a change in Ru species at the perovskites is assumable, shown in the schematic diagram of Fig.2A. Incorporation of Ru in a single-phase perovskite structure is expected until the molar ratio of Ru reaches 0.2, which could be denoted as lattice type Ru. This is shown in the trend of the d-value and cell volume in Fig.2B shows a gradual increase up to the Ru fraction of 0.2, due to the larger atomic sizes of Ru. Furthermore, these values do not change at higher Ru fractions, which may indicate a maximum amount of Ru for doping in $LaCrO_3$. Under such circumstances, the excess Ru may aggregate to the surface mostly as RuO_2, labelled as surface type Ru.

To compare the dispersion and composition of the Ru phase in the perovskite structure, SEM-EDX and TEM-EDX analysis of LCR-0.2 and LCR-0.4 perovskite hollow fibers were compared in Fig.3. From Fig.3A, it was revealed that all of the constituting elements are homogeneously distributed through out the LCR-0.2 sample on the low magnification scale employed. On the other hand, Ru species in the LCR-0.4 hollow fibers were found to aggregate in some regions, while the other elements were still homogeneously distributed. This could be a clue that excess Ru exists as a different Ru phase on the catalyst surface. The synthesized catalysts were further examined by TEM and EDX to investigate lattice *d*-space and metal composition. Fig.3B(a)

shows TEM micrographs derived from LCR-0.2 with an interplanar distance of 0.277 nm at the regular lattice fringes (112) of the perovskite structure. Identified by their acute angle, the observed data were in accordance with the phase found in XRD. Furthermore, many stacking faults and micro-twinnings of typical perovskite structures were observed. In case of the LCR-0.4 in Fig.3B(b), spherical Ru based nanoparticles with diameters of 20–30 nm were found in a separated $LaCr/RuO_2$ phase with an interplanar distance of 2.753 Å at (112). The nanoparticles on the surface showed an interplanar distance of 0.240 nm for the crystal planes of RuO_2 lattice fringes (111) direction with their characteristic acute angle.

2.2 Chemical structure analysis

Changes in the nature of the chemical bonds are evident analysed by the XPS analysis. In Figs.S3 and 4(A-B), XPS peaks corresponding to La 3d, Cr 2p, and Ru $3p_{3/2}$ were displayed respectively in detail. The binding energies and atomic ratios were determined by the peak fittings and summarized in Table S1. As expected, Ru is basically doped at the B site of the perovskite structure, no significant differences in the peak shape were observed for the La $3d_{5/2}$ doublets (La_2O_3 and $La(OH)_3$) for all $LaCr_{1-x}Ru_xO_3$ hollow fibers as shown in Fig.S3.[6a,8a] On the other hand, the Cr and Ru species were changed as the ratio changed, which may suggest a structural distortion of the B site. As from Fig.4A, the Cr $2p_{3/2}$ peaks were shifted from the low-valence (Cr^{3+}) toward the high-valence states ($Cr^{(3+\delta)+}$), but no significant change in peak shape was observed.[9a,b] Therefore, it is apparent that the portion of the Cr^{3+} decreased with an elevated proportion of $Cr^{(3+\delta)+}$ as the amount of Ru was increased, due to the sharing of the electron density with the Ru and less electronegative Cr. However, for LCR-0.4, the Cr $2p_{3/2}$ peaks were further

shifted toward the higher valence states of $Cr^{(3+\delta)+}$ with a change in the peak shape, indicating partial distortion of the typical perovskite structure. The Ru $3p_{3/2}$ peak in Fig.4B can be also used to determine the proportion of the two different Ru species of Ru^{4+} and $Ru^{(4+\delta)+}$.[8c,15a-c] From the increase in the peak intensity, the increase in the total Ru amount as designed were confirmed. About the proportion of the Ru species in Table S1, the perovskite with a Ru incorporation exhibited higher binding energy for $Ru^{(4+\delta)+}$, generally mixed-valence state, located in the BO_3 lattice rather than on the surface. The proportion of $Ru^{(4+\delta)+}$ rises incredibly for the LCR-0.4, whereas Ru^{4+} valence state relatively decreased. This partial oxidation may have occurred due to the formation of surface type Ru by the aggregation of unsubstituted Ru and exist as Ru oxides, as assumed in Fig.3.[15c]

To investigate more about the chemical bonding character of Ru by the electronic and geometric structures of absorbing ions, LCR-0.2 and LCR-0.4 hollow fibers were examined using Ru K-edge XANES and filtered/transformed EXAFS spectra. In Fig.4C, the main peaks of the XANES spectra showed similar shapes for both compounds, though small changes in the intensity and shifts in the energies were observed. No pre-edge peaks observed at the positions of the edge jump which suggests a strongly stabilized local symmetry for Ru, likely by the nearly regular octahedral symmetry at the orthorhombic lattice. In the main edge regions I and II, intense and sharp resonance peaks of the Ru species were essentially identical to those of the RuO_2 standard. In the main edge region II, the peak position for LCR-0.2 shifted to a higher energy field and further increased at the Ru portion of 0.4. The position of the peaks in the main edge regions are generally assigned to the dipole allowed $1s \rightarrow 5p$ transitions and provide indirect information on the $Ru^{(4+\delta)+}$ species.[16a-c] Because the higher effective charge of Ru mainly contributes to the increase in the transition energy, the shift to a higher energy region indicates an increase in the

proportion of $Ru^{(4+\delta)+}$ at the changed perovskite structure. This result is in good agreement with the XPS curve fitting results (Table S1).

In Fig.4D, Fourier-transformed Ru K-edge EXAFS spectra of the perovskites and references were displayed at the range of 1–6 Å. For all measured compounds, an intense and highly isotropic first peak in the R space of 1–2 Å were clearly observed, which is attributed to the ordered O symmetry of the RuO octahedron. In the higher *R* range of 2–4 Å, it is obvious that the shape of the Fourier-transformed spectra is different for the perovskites with different amounts of Ru. The peaks in this range are principally due to the second nearest neighbor (A-site cation) and third nearest neighbor (B-site cation) at the ABO_3 perovskite structure, and the corresponding collinear multiple scattering contribution.[16a,b] The collinear multiple scattering contributions via the linear Ru–O–B chain, particularly, provides a contribution for 2.5–6 Å which can be correlated with the Ru species scattering in the perovskite structure. It has been reported that the decrease in the intensity of this peak indicates a decrease in the size of the Ru species, meaning an increase in the metal dispersion in the perovskite.[16b,d] Based on such observations, the peaks of the second shell for LCR-0.2 with a lower intensity indicates that the Ru species were highly dispersed because of lattice type Ru that has strong interactions between the Ru–O–B chains. The fitting results generated from the Fourier transformation corresponding to the Ru–O bonding pair are shown in Fig.S4 and Table S2 to obtain more information about the chemical bonding characteristics. The fitted plots exhibited low R-factors which imply fair fitted results. It was clear that the bonding structure for LCR-0.4 is almost the same as the RuO_2 reference, as we assumed a surface type Ru formation. On the other hand, most of the bonding features for LCR-0.2 are different, escpecially the main Ru-O(1) bonding length of 2.01 Å (RuO_2=1.98 Å), which is due to the distorted RuO_6 octahedral bonding configuration in the perovskite structure.[16e-f]

It is also noteworthy that the oxygen species also transform into a highly active phase for the LCR-0.2. Generally, the surface adsorbed oxygen is more involved in catalytic reactions than the lattice oxygen, which can be an important factor for heavy-hydrocarbon reforming.[8b] These different oxygen species can be identified from the O XPS spectra displayed in Fig.5A. Typically, the O spectra peak is split into two peaks of lower binding energy (529.3 eV) for lattice oxygen (O^{2-}) and higher binding energy (531.3 eV) for surface adsorbed oxygen (O^{-}).[7b,9b] A higher proportion of adsorbed oxygen was observed on the surface as Ru substitution was increased until 0.2, and the spectra were used to calculate the ratio of $O_{surface}/O_{lattice}$ for each sample. The values of 0.71, 0.84, 0.92, 1.24, and 1.01 were found for LC, LCR-0.05, LCR-0.1, LCR-0.2, and LCR-0.3, respectively, while LCR-0.4 can be considered due to the dual phase from different peak shape by the moderated perovskite structure with surface type Ru, separately. The same tendency of the oxygen species was observed by the XANES analysis of the O K-edge, as shown in Fig.5B. O K-edges can be divided into two regions, corresponding to O_{α} and O_{β}, at the range of ~533 eV and ~536 eV, respectively. O_{α} is assigned as oxygen atoms located at the surface/near-surface region from a transition of an O 1s electron into unoccupied anti-bonding O 2p, and O_{β} expressed the oxygen atoms in the structural oxide phase from the convolution of O 2p states in the perovskite lattice.[17a,b] With the consistent XPS results, it was found that the surface oxygen increases as the Ru amount increases maybe due to the structural changes after Ru doping. On the other hand, sudden decreases of LCR-0.3 and LCR-0.4 were observed by the separation of the Ru species. Compare to all, LCR-0.2 possess the highest amount of active oxygen, which may provide a higher catalytic activity for the ATR reactions.

Meanwhile, the the perovskite and Ru species changes can also modify the reduction behavior of the perovskites. Therefore, H_2-TPR was carried out in Fig.5C. In general, the reduction

peak position is affected by the crystallite size, metal oxidation state or location, bonding strength, oxygen defects, and doping level of the samples.[6a,9b,18] The H_2-TPR profiles of the perovskites showed peaks corresponding to a two-step consecutive reduction. The first peak contains the reductions of Ru and Cr ions on the surface from their oxidization to the lower state. The second reduction peak at higher temperature is attributed to the reduction of Ru and Cr ions in the perovskite structure.[6a] By partial incorporation of Ru to Cr in the B-site, the first reduction peak shifted to a lower temperature. When the fraction of Ru is >0.3, a bigger peak with a larger area is observed for the first reduction below 200 °C;[18] because Ru may be located outside the perovskite lattice rather than the inner lattice. Compared to others, the second reduction peak for LCR-0.2 was seen at a higher temperature with significantly larger peak area. This result is attributed to the presence of an optimal Ru quantity incorporated into the lattice, along with the high portion of $Cr^{High\text{-}Valence}$ species that are strongly bonded to O.[9b] As a result, this fine profile for LCR-0.2 indicates enhanced reducibility with higher H_2 consumption and better structural stability compared with the other Ru-substituted samples. Therefore, it is plausible that relatively high percentages of $Ru^{(4+\delta)+}$, $Cr^{(3+\delta)+}$, and O^- species in LCR-0.2 is correlated to the formation of the lattice type Ru, which enhance the mobility of oxygen in the lattice and are related to the oxygen surface storage capacity. These compositions may demonstrate the prevalent role of Ru and Cr redox cycles on catalytic activity. Usually, heavy-hydrocarbon species are adsorbed and interact with the O atoms during ATR. Here, the electron transfer to the reactants from the active metals neighboring the vacancy at the B-site facilitates the C–H bond cracking for H_2 release. This feature is also crucial for the stability and resistance of the coke formation during the catalytic hydrocarbon reforming processes. Consequently, LCR-0.2 is expected to show the greatest activity

and stability as a redox catalyst in the reforming of heavy-hydrocarbons fuels to produce H_2 gas under harsh reaction conditions.

2.3 Heavy-hydrocarbon autothermal reforming

To evaluate the catalytic activity and stability of the prepared catalysts, ATR tests using hexadecane ($C_{16}H_{34}$) as a fuel with 100 ppm of sulfur were carried out at the operating conditions of 800 °C, 4000/h, and carbon/H_2O/O_2 = 1/1.25/0.4. The product mole percentage toward the H_2 and by-products versus time in stream over the catalysts of LCR-x (x = 0-0.4) hollow fibers are shown in Fig.6. The product production time curves displayed by the usual scattered data for reforming reaction which is due to the non-homogeneous mixture of the reactants. All hollow fibrous catalysts exhibited good reforming efficiencies for ATR using the sulfur-containing heavy-hydrocarbon. The high performance of the catalyst is not only attributed to the Ru composition which provides a great catalytic efficiency but also, due to the improved mass/heat transfer rates from the high effective surface area of the micro-tubular structures.[12] Comparing to LC, the initial activities for H_2 production are higher for the Ru-substituted catalysts, proving that the substitution of Cr by Ru favorably affects the H_2 extraction capacity from the hydrocarbon molecules. However, it was obvious that the initial amount of H_2 produced up to 10 h varied depending on the amount of Ru in the perovskite structure. Values of 38.8, 45.5, 48.6, 62.7, 63.4, and 69.7 mol% were obtained for LCR-x hollow fibers (x = 0, 0.05, 0.1, 0.2, 0.3, and 0.4), respectively, with the order of $x=0 \ll 0.05 \leq 0.1 \ll 0.2 = 0.3 < 0.4$, which are comparable with other supported noble metals for this type of reaction.[5a-c] In addition, the higher reforming capacity was accompanied by the lower proportion of non-reformed hydrocarbons (CH_4, C_2H_4,

C_2H_6, and C_3H_6) in the products from each figure in Fig.6, which indicates that the increase in H_2 production was supplemented by the decrease in CO_x formation.

From Fig.6, the stability of the prepared perovskite catalysts can be also examined against long periods on stream of heavy-hydrocarbon ATR in the presence of sulfur. Interestingly, the catalysts derived from the LCR-0.05, LCR-0.1, and LCR-0.2 hollow fibers with lattice type Ru were not suffered from the decrease in H_2 production over the same time period. As expected, the LCR-0.2 hollow fiber catalyst especially exhibited high activity and great stability with a lower degree of deactivation, which definitely shows a different behavior to the Ru supported $LaCrO_3$ catalyst with a dramatic decrease in performance at the same loading (Fig.S5). It is strongly associated with the reactivity owing to the relatively higher amount of lattice type Ru in the perovskite. Furthermore, the stable reactivity was achieved together with a high tolerance against carbon deposition and sulfur poisoning on the feeds of heavy-hydrocarbon. This result was even comparable with the reforming results using Pt-GDC (Fig.S6) where a decrease in catalytic activity was accompanied under harsh reaction conditions (fuel with C and S species), since it is usually known that a high deactivation occurs by S poisoning at the Pt metal surface.[11] The catalysts derived from LCR-0.3 and LCR-0.4 hollow fibers, having surface type Ru, show also a noticeable decrease in H_2 production of around 6% and 34%, respectively over time, even though the initial performances were relatively high. The decrease in H_2 production was also accompanied by a substantial increase in CO_2 production for the LCR-0.3 in a minor way, and especially for the LCR-0.4 with surface type Ru. This result can be explained by the increased occurrence of the Boudouard reaction ($2CO \rightleftharpoons CO_2 + C$), maybe owing to a greater formation of coke. Coking usually blocks the active sites and sinters the catalyst, which results in the loss of surface area and a reduction in the number of active surface sites.[4] Therefore, after each heavy-hydrocarbon

reforming runs, the presence of deposited carbon and sulfur on the catalytic surface may provide a clue on the stability depending on the position of the active Ru at the perovskite catalysts.

2.4 Material characterization after the catalyst tests

To investigate the deactivation behavior during heavy-hydrocarbon ATR in the presence of sulfur for 50 hr, all catalysts were post-characterized. After each ATR, different quantities of carbonaceous residue deposits on the used catalysts. The amount of the deposited carbon was calculated by TGA analysis (Fig.S7) and the results are summarized in Fig.7A. The total coke quantities for $LaCr_{1-x}Ru_xO_3$ (x = 0, 0.05, 0.1, and 0.2, respectively) were quite low and even decreased close to the order of the higher Ru amount, whereas a slight increase was observed for x=0.3 and a significant increase was observed for x=0.4. Remarkably, these results are consistent with the stability results (Fig.6), depending on the amount of Ru and its location in the active region. From the SEM results in Fig.7B, the micrographs exhibited a retained hollow fibrous architecture composed of the perovskite nanoparticle networks. No carbon deposition on LCR-0.2 surface was seen whereas an obvious covering with many carbon filaments (confirmed also from the large coke quantity in Fig.7A) was displayed on the LCR-0.4 fiber surface. From the TEM analysis of LCR-0.2 after ATR in Fig.S8A, there is also almost no carbon deposition on the surface seen without any structural change of the original and surface/bulk structures. Moreover, it is interesting that a base carbon growth was displayed due to the position of Ru inside the perovskite structure with strong interaction, which shows usually slower coke formation.[19] The presence of the deposited carbons on the perovskite catalysts can be further proved by the XRD analysis in Fig.S8B. XRD spectra of LCR-0.2 exhibited low-intensity diffraction peaks of carbon, indicating limiting effect on carbon formation. On the other hand, the XRD result for LCR-0.4 highlights a large amount of carbonaceous from a huge peak of graphitic carbons (JCPDS 75-1621)[4b,c]. The

structural change of the used LCR-0.4 catalysts was also indicative through the XRD with a change in the *d*-value and unit cell parameters after the long reaction time (Table S3). Moreover, the Ru species of the LCR-0.4 outside the catalyst as a tetragonal RuO_2 (Fig.1B) partially changes to metallic Ru at the reductive reaction environment, which may be a factor in the increased coke formation and sulfur poisoning through the strong bonding with Ru metal.[11,19]

The change in the Ru chemical structure after the heavy-hydrocarbon reforming was easily detectable by the Ru K-edge XANES and filtered/transformed EXAFS spectra, as shown in Fig.8A-B. From the XANES spectra in Fig.8A, no changes of the peak shape and proportion of $Ru^{4+}/Ru^{(4+\delta)+}$ species in the LCR-0.2 after ATR were visible. Furthermore, there was no reflection on the pre-edge, which means a stable local symmetry in the orthorhombic structure. Compared to the LCR-0.4 after ATR, a weak pre-edge jump in region I was clearly observed at around 22150 eV. Generally, pre-edge peaks are due to the dipole forbidden 1*s*–4*d* transition, which can explain a broken O symmetry of the LCR-0.4 during the harsh ATR reaction.[16a,b] When the pre-edge peaks become intensified because of d–p mixing or the quadruple allowed transition, O_h symmetry is broken as the distortion of the Ru species from O symmetry around the absorber increases. The peak at the main edge region II was also different and reflected a change in the original perovskite structure to the separated RuO_2 species. To obtain more information about the change in the chemical bonding characteristics, the fitting results generated from the Fourier transformation, are shown in Fig.8B corresponding to the Ru–O bonding pair. The fitted Ru K-edge EXAFS spectra for LCR-0.2 do not change at all after the ATR test. However, in the fitted Ru K-edge EXAFS spectra for LCR-0.4, the highly isotropic peaks became smooth and collinear multiple scattering in the whole R space disappeared, which may reveal the broken ordered O symmetry of the RuO_6 octahedron and linear Ru–O–B chain, respectively.

XANES spectra for each carbon and sulfur in Fig.8C-D can serve as evidences to prove the carbon/sulfur deposition mechanism of the lattice and surface type Ru. Fig.8C shows the C K-edge XANES spectra overlapping with the Ru $M_{5,4}$-edge. Firstly, the existence of Ru in both LCR perovskites is clear by the shoulder at 283.5 eV assigned to Ru M_5-edge.[20a,b] In the case of C K-edge, two distinct peaks, assigned as graphite π^* and σ^* transitions at ~285.5 eV and ~291.9 eV respectively, are observed even for the small amount of carbon coking occurred at LCR-0.2. Yet, the intensity for LCR-0.4 was much higher than the LCR-0.2, due to the higher carbon deposit. The most interesting feature is the bigger peak intensity of a new peak at ~289.6 eV for LCR-0.4, indicating a stronger oxidized C environment than that for –COOH in the deposited carbon.[20b] Therefore, it could be interpreted to a strong interaction with the surface type Ru through chemical bonding with the produced carbon species. Similar results were seen at the S L-edge XANES spectra in Fig.8D. The peak intensity for LCR-0.4 was essentially bigger than LCR-0.2, demonstrating a larger amount of poisoned surface by sulfur. Moreover, the spectra for LCR-0.4 shows three different peaks in the 161-168 eV region.[20c,d] Each arising peaks by several electronic transitions exactly matched with the used precursor of DPT in the fuel, specifying sulfur poisoning through a strong binding with the Ru surface which could turn also to a carbon growth site.[4] Remarkably, a positive shift of the main peaks was observed for LCR-0.2 with also an intensity decrease. The positive shift reveals oxidation of the sulfur species to a gas phase like SO_x, which might be promoted by the oxygen activation from the high amount of surface oxygen.[7b,9b] This mechanism for LCR-0.2 hollow fiber catalyst provides another understanding of the slow deactivation during the heavy-hydrocarbon reforming with sulfur species.

2.5 Expected reaction mechanism.

Summing up all the results, we could finally come to the reaction mechanism of the surface/lattice type Ru and lattice type Ru. The comparisons are illustrated in Fig. 8E for the autothermal reforming by heavy-hydrocarbon fuel in the presence of sulfur. It was found that the deactivation of the surface/lattice type Ru is mainly caused by carbon coking and sulfur poisoning, which can be also the reason for the low durability of the Ru supported perovskite catalyst. Especially, carbon coking usually comes from the cracking of the carbon chain in the fuel, which is more likely when heavy-hydrocarbon fuel used. Ideally, the hydrocarbon species are adsorbed on the surface of the active metal site and converts to H_2 and CO_x by reaction with O_2 and H_2O molecule. However, from the strong interaction of the metallic surface Ru species, the stabilization step of the active precursor was carried out to form filamentous coke (C*+C*).[11b,c, 19] The large sulfur poisoning was also due to the strong binding energy of Ru-S, which were accelerated by the change in the oxide symmetric and Ru species. On the contrary, the lattice type Ru fully doped in perovskites shows less carbon coking and sulfur poisoning. As it is very important to transform coke precursors (C*) into gases for example by the Boudouard reaction ($C^*+CO_2 \leftrightarrow 2CO$), gasification ($C^*+H_2O \rightarrow CO+H_2$) and methanation ($C^*+2H_2 \leftrightarrow CH_4$), the catalyst with lattice type Ru shows sufficient activity.[11] Moreover, the fully doped perovskite catalysts possess much more active oxygen by oxygen defects, which enhances the formation of C–O active bonds to minimize C–C bond formation. In the case of sulfur poisoning, the lattice type Ru has also lower binding energy with sulfur species and the active oxygen provides a reactivity to oxidize the S species to gaseous SO_x.[4b,11a] This mechanism suggests that the nature of Ru species inside the perovskite lattice has enough activity to crack the heavy-hydrocarbons that possess unsaturated C=C bonds by having high coordination ability. Furthermore, this protects the catalyst from carbon coking and even sulfur poisoning for great catalytic stability.

3. Conclusions

In this work, hollow fibers networked with perovskite nanoparticles of $LaCr_{1-x}Ru_xO_3$ (x = 0–0.4) were perpared, which have a favorable effect on the capacity to yield H_2 directly from heavy-hydrocarbon fuel reforming. The most important findings arrived at: (i) At the Ru amount of 0.05–0.2, lattice type Ru was dominant whereas surface type Ru was formed at the higher Ru amount of 0.3-0.4. (ii) Partial substitution of Cr by Ru in the perovskite lattice led to the strucutral modification which had a positive influence on the enhanced catalytic property through more surface oxygen and better reducibility. (iii) From the characterization after ATR reactions, the stability of the perovskite structure was affected by the difference in the Ru chemical nature. The formation of surface nanometric Ru particles was the factor in the accumulation of carbon and sulfur on the catalyst surface due to the strong metal–C/S chemical bonding, which is related to the decrease in the H_2 production and increase of the CO_2 by-product. (iv) The optimal composition of LCR-0.2 hollow fiber, having only lattice type Ru, showed comparable activity and was less prone to deactivation by coke and sulfur deposits, through the inner location of the active sites and structural distortion with more active oxygens at the surface. These highly active and durable catalyst materials could possibly be applied to the actual reforming process that is being constructed for the infrastructure in the upcoming H_2 society.

4. Experimental details

4.1 Synthesis of Hollow Perovskite Fiber Catalysts

Synthesis procedure of the hollow $LaCr_{1-x}Ru_xO_3$ fiber was shown in the Fig.1 [12]. The perovskite hollow fiber ($LaCr_{1-x}Ru_xO_3$, x=0, 0.05, 0.1, 0.2, 0.3, and 0.4) was prepared using aqueous (solution) impregnation synthesis which is a rapid and convenient method to provide high

surface area oxides. The acid-treated ACF template (1 g) with H_2SO_4 (6 M) and HNO_3 (6 M) was immersed in a water based solution of $La(NO_3)_3 \cdot 9H_2O$, $Cr(NO_3)_3 \cdot 9H_2O$, and $HN_4O_{10}Ru$ with a certain stoichiometric La^{III}, Cr^{III}, and Ru^{III} ions, resulting in ionic binding of the metal cations to the negatively charged surface of the ACF. After washing with deionized water for 24 hours, the hollow fiber composed of a perovskite nanoparticle network could then be successfully formed by mild heat treatment of the ACF impregnated with $La^{III}/Cr^{III}_{1-x}/Ru^{III}_x$ (x=0, 0.05, 0.1, 0.2, 0.3, and 0.5) ions at 1027 K for 6 h in sufficient air flow to remove the C content via combustion with a formation of crystalline structure. For comparison, Ru supported $LaCrO_3$ (Same Ru loading with LCR-0.2) and 5wt.% Pt–GDC (gadolinium-doped CeO_2) catalysts were prepared by incipient wetness impregnation in a similar manner [2b].

4.2 Synthesis of Catalyst characterization

The chemical composition of each sample was analyzed by Inductively Coupled Plasma-Atomic Emission Spectroscopy (ICP-AES, OPTIMA 4300DV, Perkin-Elmer, USA). For crystal structure analysis, X-ray diffraction (XRD) was performed by a Rigaku Miniflex AD11605 with X-ray diffractometer using Cu Kαradiation (λ= 1.5405 nm) at 30 kV and 30 mA. The morphology of the as-synthesized samples was monitored by using scanning electron microscope (SEM, JEOL JSM-6701F) operated at 15 kV, equipped with a an energy-dispersive X-ray (EDX) spectrometer. High-resolution transmission electron microscopy (HR-TEM) imaging as well as selected area electron diffraction (SAED) was performed at 200 kV in a JEOL JEM-2100F with an energy-dispersive X-ray (EDX) spectrometer. The BET (Brunauer-Emmett-Teller) surface area, pore volume and pore diameter were determined by a distribution graph of N_2 adsorption-desorption at 77 K (Micromeritics ASAP 2010), using the BET equation. To probe the chemical states of the elements and their proportions on the surface of the perovskites, the X-ray photoelectron

spectroscopy (XPS) were recorded on a K-alpha (Thermo VG, U.K.) equipped with Al monochromated X-ray sources (Al Kα, 1486.6 eV), using a hemispherical energy analyzer. The samples were fixed on a carbon tape and all binding energies were calibrated using C1s (284.8 eV). The catalytic sites of the perovskites were examined by temperature programmed reduction (TPR; Belcat-M) equipped with a thermal conductivity detector (TCD). The catalyst samples (15 mg) were heated from room temperature to 900 ^{o}C at a rate of 10 ^{o}C/min under the gas feed rate of 40 cc/min (10% H_2/Ar). The X-ray absorption spectroscopy (XAS) results were recorded at the Pohang Accelerator Laboratory (PAL, Pohang, Korea), beamline 10C (Multipole-wiggler, Ge 13-element detector) and 10D (Bending magnet, Phoibos 150). Measurements were made at room temperature with solid samples. The X-ray absorption near edge structure (XANES) data of O K-edge were collected at beamline 10D XAFS. The XANES and extended X-ray absorption fine structure (EXAFS) data at Ru K-edges before and after the samples were collected using thin layers of powder samples deposited on transparent adhesive tape. The measurements were performed in transmission mode at beamline 10C Wide XAFS using gas-ionization detectors. All the spectra were calibrated by first measuring the spectrum of RuO_2, $RuCl_3$ and Ru metal references.

4.3 Catalytic Testing

The autothermal reforming of heavy hydrocarbon was carried out at atmospheric pressure in a fixed-bed stainless steel flow reactor with 8 mm internal diameter. The temperature of the reactor was monitored and controlled by thermocouples that were coaxially inserted into the center of the catalyst bed. The fuel in this study was hexadecane (Aldrich) with a high carbon number of 16, including DPT (Dibenzothiophene, Sigma-Aldrich) of 100ppm for the sulfur species. The fuels were injected by liquid pump and ultrasonic injector for homogeneous fuel supply. For ATR experiments of the hollow fiber catalysts, each feed, with a change of the molar ratios of H_2O/C =

1−3/1 and O_2/C = 0.3−0.7/1, was introduced into the reactor by a mass flow controller (GHSV = 2000−5000 h^{-1}), where the temperatures was varied to 700−850 ^oC at the atmospheric pressure. With an optimum operation conditions, the reforming reaction of each hollow fiber catalysts was carried out for 50 h. All reformates (H_2, CO_2, CO, CH_4, $C_{2,3}H_n$) were periodically measured using on-line GC (Youglin-6000) equipped with a TC detector and an FI detector which were programmed to operate under high-sensitivity conditions, and the product distributions were averaged from the steady state. The conversion and H_2 mole percentage of products by hexadecane are defined as follows:

- Hexadecane conversions at the liquid base were over 99%.

- Product distribution: (%) (i: H_2, CO, CH_4, CO_2, $C_{2,3}H_n$ (C_2H_4+C_2H_6+C_3H_6)):

$$\frac{(mole \quad i)_{out}}{\sum mole \quad i_{out}} \times 100$$

ACKNOWLEDGMENT

This research was supported by the Industrial Technology Innovation Program funded by the Ministry of Trade, Industry and Energy (MOTIE), Republic of Korea (grant number 10052076).

REFERENCES

[1] (a) A.G. Bhavani, W.Y. Kim, J.S. Lee, *ACS Catal.,* 3(7) (2013) 1537–1544. (b) D. Baudouin, K. C. Szeto, P. Laurent, A. Mallmann, B. Fenet, L. Veyre, U. Rodemerck, C. Copéret, C. Thieuleux, *J. Am. Chem. Soc.* 134 (2012) 20624–20627.

[2] (a) R. M. Navarro, M. C. Álvarez-Galván, M. Mota, J. A. Villoria de la Mano, S. M. Al-Zahrani, J. L. G. Fierro, *ChemCatChem* 3 (2011) 440–457. (b) I. Kang, J. M. Bae, G. J. Bae, *J. Power Sources* 163 (2006) 538–546.

[3] (a) G. Nahar, V. Dupont, *Recent Patents on Chemical Engineering*, 6 (2013) 8–42. (b) M. A. Reese, S. Q. Turn, H. Cui, *J. Power Sources* 195 (2010) 553–558.

[4] (a) Y. Chen, C. Xie, Y. Li, C. Song, T. B. Bolin, *Phys. Chem. Chem. Phys.*, 12 (2010) 5707–5711. (b) C. Xie, Y. Chen, M. H. Engelhard, C. Song, *ACS Catal.*, 2 (2012) 1127–1137. (c) E. Nikolla, A. Holewinski, J. Schwank, S. Linic, *J. Am. Chem. Soc.* 128 (2006) 11354–11355.

[5] (a) R. K. Kaila, A. Gutierrez, Q. I. Krause, *Appl. Catal. B. Environ.*, 84 (2008) 324–331. (b) M. C. Alvarez-Galvan, R. M. Navarro, F. Rosa, Y. Briceno, F. Gordillo Alvarez, J. L. G. Fierro, *Int. J. Hydrogen Energy* 33 (2008) 652–663. (c) X. Karatzas, K. Jansson, A. González, J. Dawody, A. Svensson, L. Pettersson, *Appl. Catal. B-Environ.* 101 (2011) 226–238.

[6] (a) N. Mota, M. C. Alvarez-Galván, R. M. Navarro, S. M. Al-Zahrani, A. Goguet, H. Daly, W. Zhang, A. Trunschke, R. Schlögl, J. L. G. Fierro, *Appl. Catal. B-Environ.* 113 (2012) 271–282. (b) J. R. Mawdsley, J. T. Vaughey, T. R. Krause, *Chem. Mater.* 21 (2009) 4830–4838. (c) A. Qia, S. Wang, G. Fu, C. Ni, D. Wu, *Appl. Catal. A-Gen.* 281 (2005) 233–246.

[7] (a) J. Sfeir, P. A. Buffat, P. Mockli, N. Xanthopoulos, R. Vasquez, H. J. Mathieu, J. V. herle, K. R. Thampi, *J. Catal.* 202 (2001) 229–244. (b) K. Rida, A. Benabbas, F. Bouremmad, M. A. Peña, E. Sastre, A. Martínez-Arias, *Appl. Catal. A-Gen.* 327 (2007) 173–179.

[8] (a) M. A. Pena, J. L. G. Fierro, *Chem. Rev.* 101 (2001) 1981–2017. (b) R. J. H. Voorhoeve, D. W. Johnson, J. P. Remeika, P. K. Gallagher, *Science* 4 (1977) 827–833. (c) J. Suntivich, H. A. Gasteiger, N. Yabuuchi, H. Nakanishi, J. B. Goodenough, Y. Shao-Horn, *Nat. Chem.* 3 (2011) 546–550. (d) S. Ida, C. Ogata, M. Eguchi, W. J. Youngblood, T. E. Mallouk, Y. Matsumoto, *J. Am. Chem. Soc.* 130 (2008) 7052–7059.

[9] (a) N. Mota, M. C. A lvarez-Galvan, S. M. Al-Zahrani, R. M. Navarro, J. L. G. Fierro, *Int. J. Hydrogen Energy* 37 (2012) 7056–7064. (b) D. Fino, N. Russo, E. Cauda, G. Saracco, V. Specchia, *Catal. Today* 114 (2006) 31–39. (c) S. Gaur, D. Pakhare, H. Wu, D. J. Haynes, J. J. Spivey, *Energ. Fuels* 26 (2012) 1989–1998.

[10] (a) P. Munnik, P. E. de Jongh, K. P. de Jong *Chem. Rev.* 115 (2015) 6687−6718. (b) D. Li, X. Li, J. Gong, *Chem. Rev.* 116 (2016) 11529−11653.

[11] (a) C. Gillan, M. Fowles, S. French, S. D. Jackson, *Ind. Eng. Chem. Res.* 52 (2013) 13350−13356. (b) S. L. Lakhapatri, M. A. Abraham, *Catal. Sci. Technol.* 3 (2013) 2755–2760. (c) S. De, J. Zhang, R. Luque, N. Yan, *Energy Environ. Sci.* 9 (2016) 3314–3347.

[12] (a) Y. Jeon, D. H. Park, J. I. Park, S. H. Yoon, I. Mochida, J. H. Choy, Y. G. Shul, *Sci. Rep.* 3 (2013) 2902. (b) Y. Jeon, C. Lee, J. Rhee, G. Lee, J. H. Myung, M. Park, J. I. Park, H. Einaga, Y. G. Shul, *Fuel* 187 (2017) 446–456. (c) Y. Jeon, H. Kim, C. Lee, S. Lee, S. Song, Y. G. Shul, *Fuel* 207 (2017) 493–502.

[13] J. Sunarso, A. A. J. Torriero, W. Zhou, P. C. Howlett, M. Forsyth, *J. Phys. Chem. C* 116 (2012) 5827–5834.

[14] R. D. Shannon, *Acta Cryst.* A32 (1976) 751–767.

[15] (a) X. Ma, R. Lin, C. Beuerle, J. E. Jackson, S. O. Obare, R. Ofoli, *Nanotechnology* 25 (2014) 045701. (b) S. Petrovic, V. Rakic D.M. Jovanovic, A.T. Baricevic, *Appl. Catal*. *B*. 66 (2006) 249–257. (c) M. Lü, M. Deng, J.C. Waerenborgh, X. Wu, J. Meng, *Dalton Trans.* 41 (2012) 11507–11518.

[16] (a) K. Getty, M. U. Delgado-Jaime, Kennepohl, P. *Inorg. Chim. Acta,* 361 (2008) 1059–1065. (b) Y. Masuda, S. Hosokawa, M. Inoue, *J. Ceram. Soc. Jpn.* 119 (2011) 850. (c) I. Arcon, A. Bencan, A. Kodre, M. Kosec, *X-Ray Spectrom.* 36 (2007) 301–304. (d) J. Y. Kim, S. H. Hwang, S. J. Kim, G. Demazeau, J. H. Choy, H. Shimada, *J. Synchrotron Rad.* 8 (2001) 722–724. (e) M. Retuerto, L. Pascual, F. Calle-Vallejo, P. Ferrer, D. Gianolio, A. G. Pereira, Á. García, J. Torrero, M. T. Fernández-Díaz, P. Bencok, M. A. Peña, J. L. G. Fierro, Sergio Rojas, *Nat. comm.* 10 (2019) 2041. (f) H. T. Jeng, S. H. Lin, C. S. Hsue, *Phys. Rev. Lett.* 97 (2006) 067002–067001.

[17] (a) Z. Wang, L. Wu, J. Zhou, Z. Jiang, B. Shen, *Nanoscale* 6 (2014) 12298–12302. (b) W. T. Hong, K. A. Stoerzinger, B. Moritz, T. P. Devereaux, W. Yang, Y. Shao-Horn, *J. Phys. Chem. C* 119 (2015) 2063−2072.

[18] D. L. Hoang, A. Dittmar, J. Radnik, K. W. Brzezinka, K. Witke, *Appl. Catal., A*. 239 (2003) 95−110.

[19] (a) A. Sacco, J. C. Caulmare, *ACS Symposium Series*, 202 (1983) 177–192. (b) Y.H. Lai, Y.L. Chen, Y. Chi, S. Liu, A.J. J. Carty, S.M. Peng, G.H. Lee, *J. Mater. Chem.* 13 (2003) 1999−2006.

[20] (a) J. Zhou, J. Wang, H. Fang, C. Wu, J. N. Cutlera, T. Kong Sham, *Chem. Commun.* 46 (2010) 2778–2780. (b) J. Yang, J. Wang, Y. Tang, D. Wang, X. Li, Y. Hu, R. Li, G. Liang,

T. Shamb, X. Sun, *Energy Environ. Sci.* 6 (2013) 1521–1528. (c) F. Jalilehvand, *Chem. Soc. Rev.,* 2006, 35, 1256. (d) Z. Wang, J. Wang, T. Sham, S. Yang, *Nanoscale* 6 (2014) 9783–9790.

Scheme, Figures and Tables

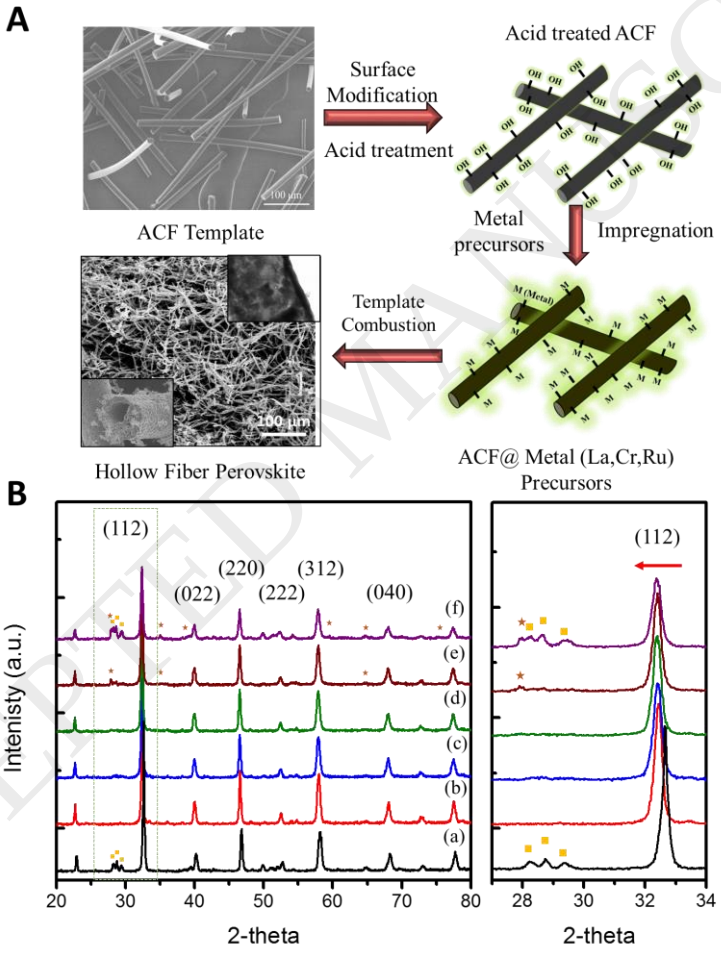

Figure 1. A. synthesis of the hollow perovskite fiber catalysts and B. XRD patterns and evolution of phases of the $LaCr_{1-x}Ru_xO_3$ hollow fibers: (a) x=0, (b) x=0.05, (c) x=0.1, (d) x=0.2, (e) x=0.3 and (f) x=0.4. (■: monoclinic La_2O_3, ★: tetragonal RuO_2).

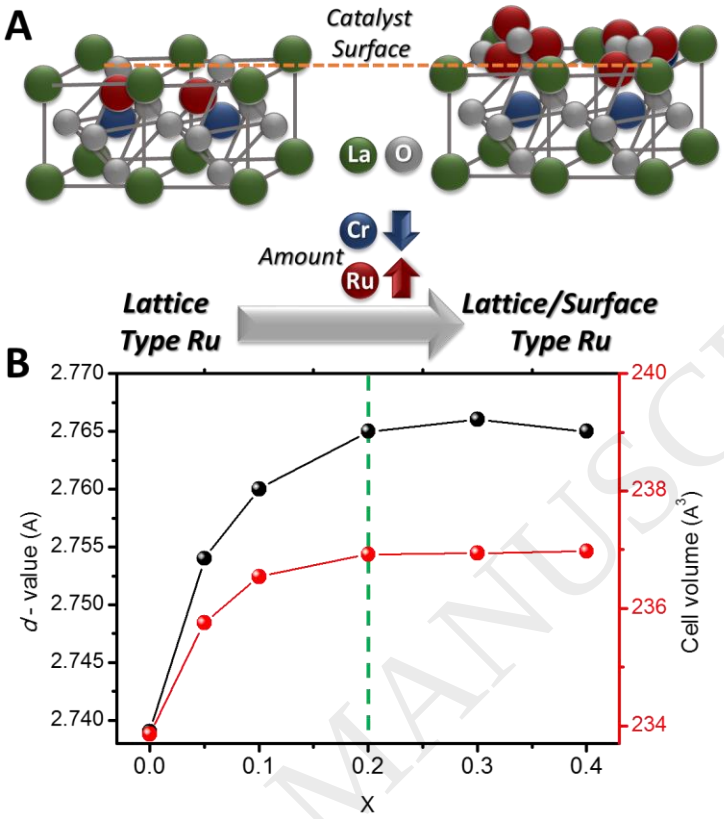

Figure 2. A. Schematic figure of the expected surface and lattice type Ru features, and the correlation of the d-value and cell volume depending on the Ru amount in the $LaCr_{1-x}Ru_xO_3$ material system.

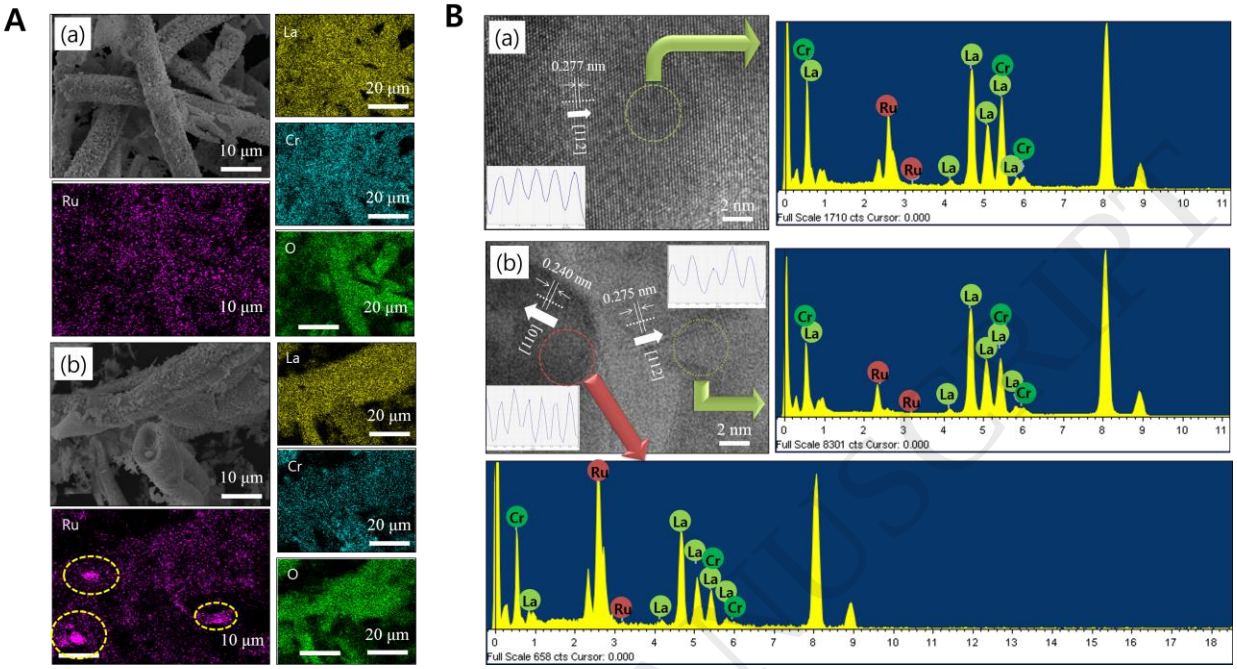

Figure 3. A. SEM-EDX mapping images and B. TEM images with a TEM-EDX of the LCR-0.2 and LCR-0.4 hollow fibers.

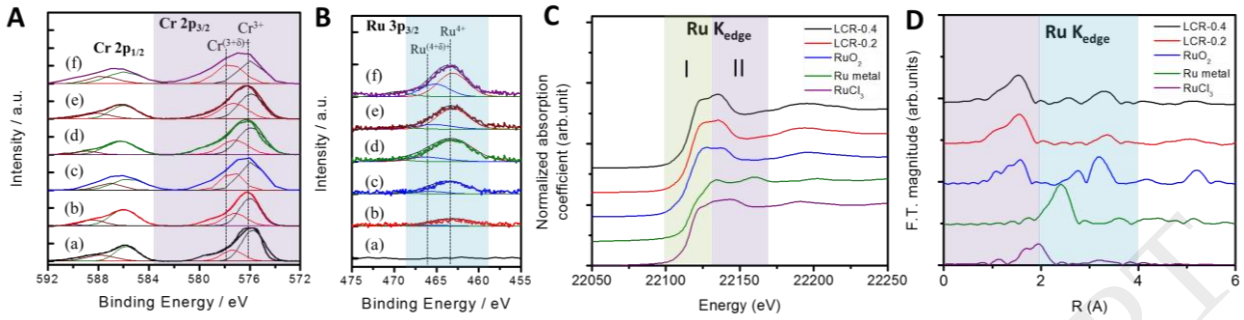

Figure 4. XPS spectra of A. Cr $2p_{3/2}$, and B. Ru $3p_{3/2}$, of the $LaCr_{1-x}Ru_xO_3$ hollow fibers: (a) x=0, (b) x=0.05, (c) x=0.1, (d) x=0.2, (e) x=0.3 and (f) x=0.4. XAS analysis of C. the normalized XANES spectra of Ru K-edge and D. Fourier-transformed EXAFS spectra of LCR-0.2 and LCR-0.4 hollow perovskite fibers, comparing with RuO_2, Ru metal and $RuCl_3$ references.

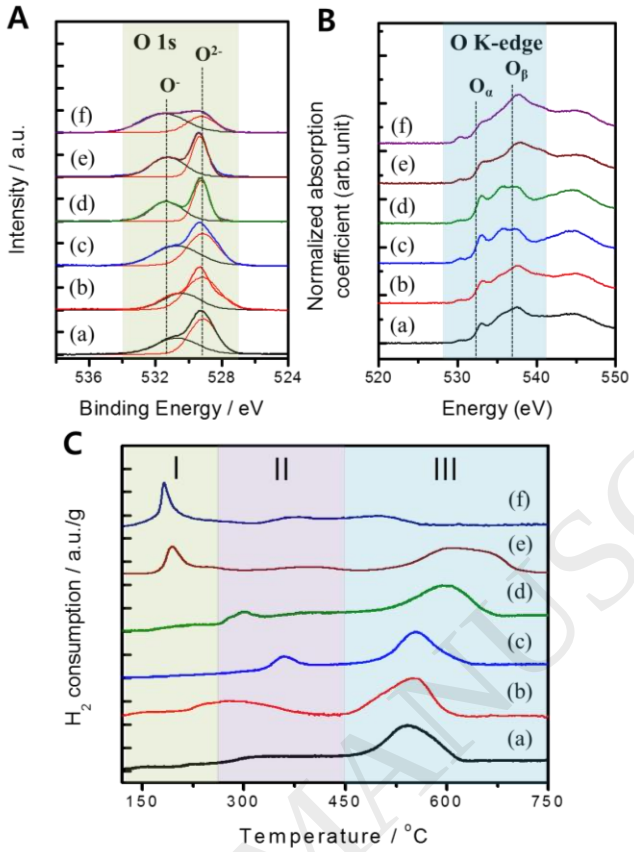

Figure 5. A. XPS spectra of O1s, B. normalized O K-edge XANES spectra and C. H_2–TPR profiles are also shown for the $LaCr_{1-x}Ru_xO_3$ hollow fibers: (a) x=0, (b) x=0.05, (c) x=0.1, (d) x=0.2, (e) x=0.3 and (f) x=0.4.

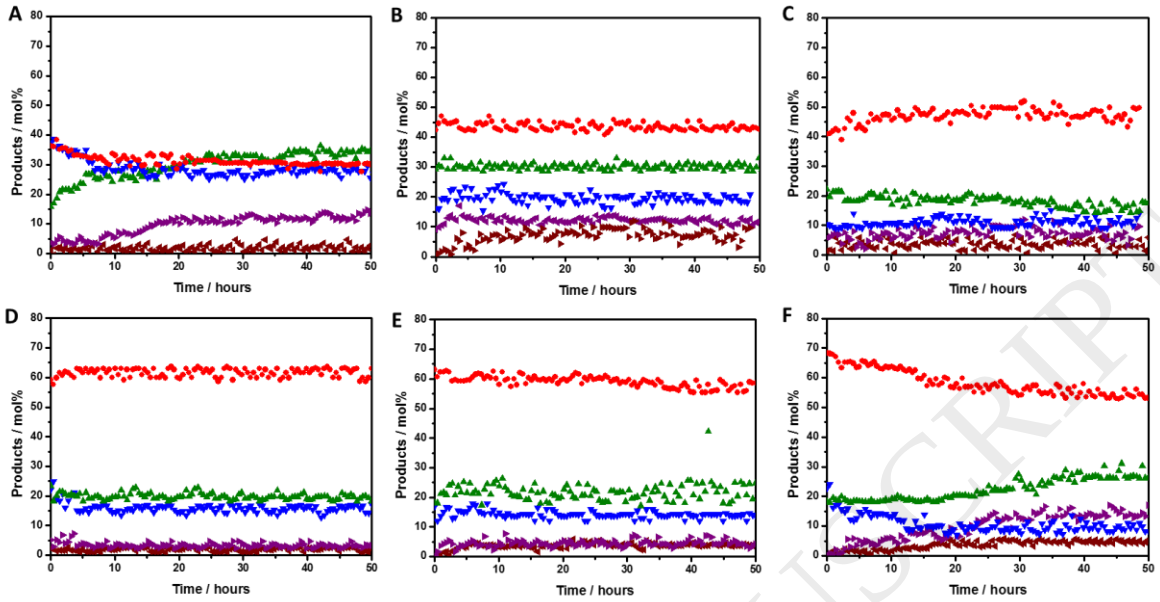

Figure 6. Products distribution (mol %) of as-prepared perovskite catalysts for ATR reaction using hexadecane ($C_{16}H_{34}$) with an addition of sulphur, Dibenzothiophene, at content of 100 ppm: $LaCr_{1-x}Ru_xO_3$ hollow fibers A. x=0, B. x=0.05, C. x=0.1, D. x=0.2, E. x=0.3, and F. x=0.4 ($C_{16}H_{34}$ = 0.012 ml·min^{-1}, $H_2O/O_2/C$=1.25/0.4/1, 800 ºC, GHSV = 4000 h^{-1}). (H_2: ●, CO_2:▲, CO:▼, CH_4: ▶, and C_2-C_3:◀).

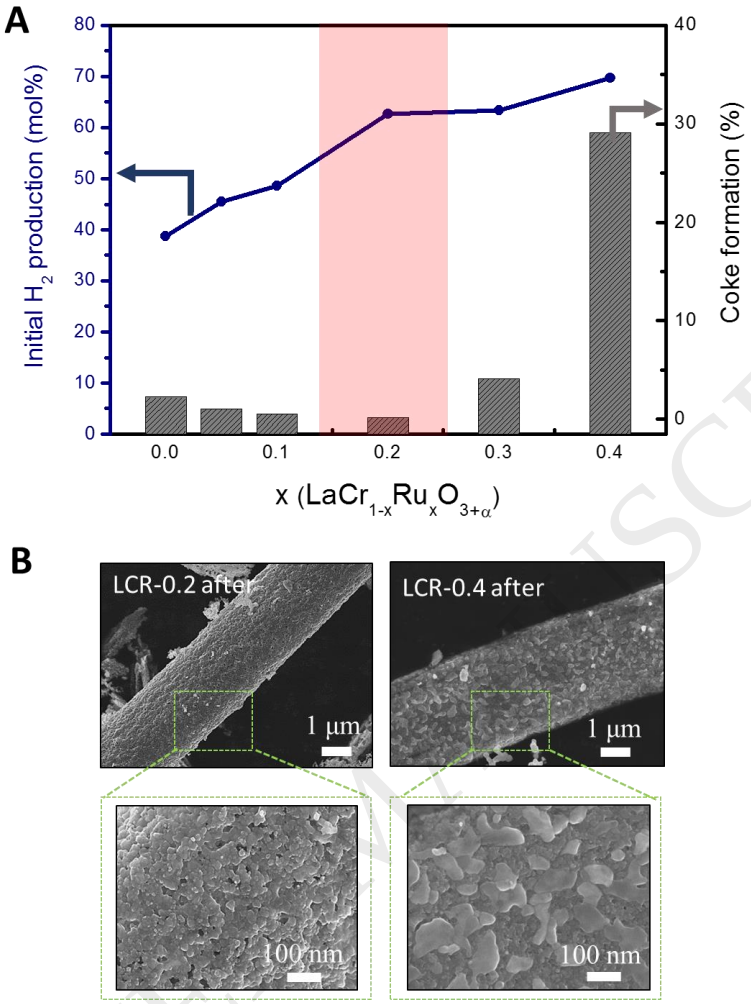

Figure 7. A. the relationship between initial H_2 production and amount of carbon deposition calculated by TGA analysis (Fig. S5) depending on the Ru doping amount, B. SEM images of the hollow perovskite fibers before/after the ATR for 50 hours.

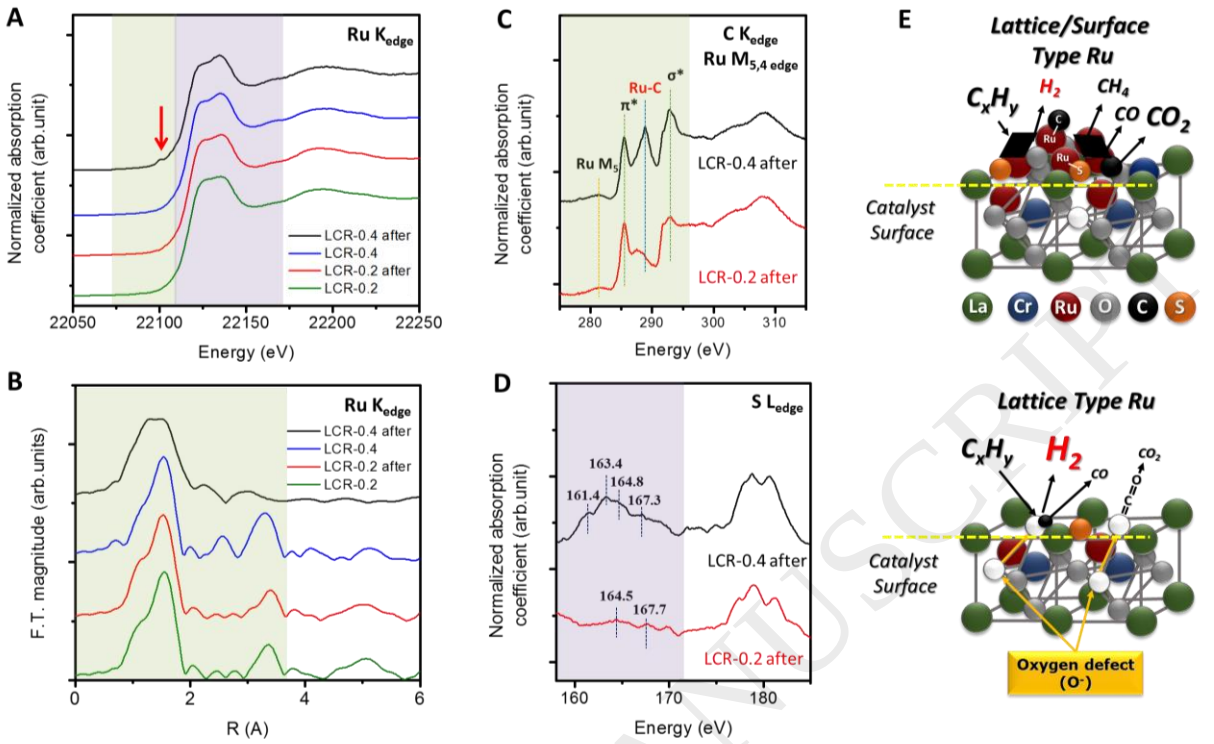

Figure 8. A. Ru K-edge XANES spectra, B. Fourier transformed Ru K-edge EXAFS spectra, C. C K-edge+Ru $M_{2,3}$-edge XANES spectra, D. S L-edge XANES spectra of LCR-0.2 and LCR-0.4 hollow perovskite fibers before/after the ATR for 50 hours, and the presumed reaction and deactivation (coke formation and sulfur poisoning) mechanism of lattice/surface type Ru doped perovskites.

Table 1. Elemental analysis, d-values, cell parameters, particles size and N_2 adsorption isomers of the $LaCr_{1-x}Ru_xO_3$ hollow fibers: (a) x=0, (b) x=0.05, (c) x=0.1, (d) x=0.2, (e) x=0.3 and (f) x=0.4.

	Elemental composition			d-value, cell parameters and particles size from XRD analysis						N_2 adsorption isomers		
	La	Cr	Ru	*a* (Å)	*b* (Å)	*c* (Å)	V_c[a] (Å^3)	*d* (Å)	P_s[b]	S_a[c]	V_T[d]	P_a[e]
(a)	1.01	0.99	-	5.499	5.485	7.762	233.86	2.739	26.9	8.4	0.033	12.3
(b)	0.98	0.93	0.07	5.506	5.505	7.784	235.95	2.754	20.7	12.6	0.046	15.2
(c)	1.00	0.90	0.12	5.512	5.512	7.788	236.64	2.760	20.2	13.3	0.049	15.2
(d)	1.00	0.80	0.19	5.517	5.513	7.790	236.92	2.764	18.3	14.4	0.051	15.9
(e)	0.97	0.66	0.32	5.517	5.513	7.791	236.94	2.766	18.5	13.7	0.050	15.4
(f)	0.93	0.55	0.43	5.519	5.511	7.791	236.97	2.765	23.3	12.7	0.044	16.8

[a] Cell volume (Å^3), [b]Particle size (nm) calculated from the most intense and non-overlapped XRD peak (112) using the Scherrer equation, [c]BET surface area (m^2/g), [d]Total pore volume (p/p0=0.927), [e]Average pore diameter (nm).